

Copper-Nickel Nitride Nanosheets as Efficient Bifunctional Catalysts for Hydrazine-assisted Electrolytic Hydrogen Production

Zhaoyang Wang, Lin Xu, Fuzhi Huang, * Longbing Qu, Jiantao Li, Kwadwo Asare Owusu, Ziang Liu, Zifeng Lin, Binhua Xiang, Xiong Liu, Kangning Zhao, Xiaobin Liao, Wei Yang, Yi-Bing Cheng, Liqiang Mai*

Z. Y. Wang, Prof. L. Xu, Prof. F. Z. Huang, J. T. Li, K. A. Owusu, Z. A. Liu, Z. F. Lin, B. H. Xiang, X. Liu, K. N. Zhao, W. Yang, Prof. Y. B. Cheng and Prof. L. Q. Mai

State Key Laboratory of Advanced Technology for Materials Synthesis and Processing, Wuhan University of Technology, Hubei, Wuhan 430070, P. R. China

E-mail: fuzhi.huang@whut.edu.cn; mlq518@whut.edu.cn

L. B. Qu

Department of Mechanical Engineering, University of Melbourne, Parkville, VIC 3010, Australia

X. B. Liao

State Key Laboratory of Silicate Materials for Architectures, Wuhan University of Technology, Wuhan 430070, P. R. China

Prof. Y. B. Cheng

ARC Centre of Excellence in Exciton Science, Monash University, Clayton, Victoria 3800, Australia

This is the author manuscript accepted for publication and has undergone full peer review but has not been through the copyediting, typesetting, pagination and proofreading process, which may lead to differences between this version and the [Version of Record](#). Please cite this article as [doi: 10.1002/aenm.201900390](https://doi.org/10.1002/aenm.201900390).

This article is protected by copyright. All rights reserved.

Keywords: water electrolysis, bifunctional catalysts, copper-nickel nitride, hydrogen evolution, hydrazine oxidation

Abstract: Electrocatalytic water splitting is one of the sustainable and promising strategies to generate hydrogen fuel but still remains a great challenge because of the sluggish anodic oxygen evolution reaction (OER). A very effective approach to dramatically decrease the input cell voltage of water electrolysis is to replace the anodic OER with hydrazine oxidation reaction (HzOR) due to its lower thermodynamic oxidation potential. Therefore, developing the low-cost and efficient HzOR catalysts, coupled with the cathodic hydrogen evolution reaction (HER) is tremendously important for energy-saving electrolytic hydrogen production. Herein, a new-type copper-nickel nitride ($\text{Cu}_1\text{Ni}_2\text{-N}$) with rich $\text{Cu}_4\text{N}/\text{Ni}_3\text{N}$ interface is rationally constructed on the carbon fiber cloth. The three-dimensional electrode exhibits extraordinary HER performance with an overpotential of 71.4 mV at 10 mA cm^{-2} in 1.0 M KOH, simultaneously delivering an ultralow potential of 0.5 mV at 10 mA cm^{-2} for HzOR in 1.0 M KOH/0.5 M hydrazine electrolyte. Moreover, the electrolytic cell utilizing the synthesized $\text{Cu}_1\text{Ni}_2\text{-N}$ electrode as both the cathode and anode displays a cell voltage of 0.24 V at 10 mA cm^{-2} with an excellent stability over 75 h. The present work develops the promising copper-nickel-based nitride as a bifunctional electrocatalyst through hydrazine-assistance for energy-saving electrolytic hydrogen production.

Author Manuscript

This article is protected by copyright. All rights reserved.

1. Introduction

With the fast fossil fuel exhaustion and associated increasingly serious environmental pollution, it is very urgent to explore green and renewable energy resources in order to deal with this situation.^[1-2]

Hydrogen with high energy density has been regarded as an ideal alternative energy carrier due to its purity and sustainability.^[3-4] Production of hydrogen by electrochemical water splitting in alkaline electrolyte which involves two half reactions, namely, the hydrogen evolution reaction (HER, $4\text{H}_2\text{O} + 4\text{e}^- \rightarrow 2\text{H}_2 + 4\text{OH}^-$) and oxygen evolution reaction (OER, $4\text{OH}^- \rightarrow \text{O}_2 + 2\text{H}_2\text{O} + 4\text{e}^-$), seems a promising and environmentally benign approach.^[5-7] At present, precious metal electrocatalysts, such as platinum-based and iridium or ruthenium-based materials are regarded as the state-of-the-art catalysts for HER and OER, respectively.^[8-10] However, the high cost, low abundance and poor stability of these catalysts significantly hinder their extensive applications in commercial electrolyzers.

Consequently, extensive studies have been conducted to develop low-cost, high-activity electrocatalysts based on transitional metal materials, including metal alloys,^[11-12] chalcogenides,^[13-17] phosphides,^[18-22] carbides,^[23-25] and nitrides^[26-31] for HER, and metal oxides,^[32-33] hydroxides,^[34] oxyhydroxides,^[35-36] selenides^[37-41] and perovskites^[42] for OER. Nevertheless, the operation voltage of water splitting in alkaline electrolyte at 10 mA cm^{-2} is still larger than 1.4 V because of the sluggish anodic OER kinetics.^[18-20, 34] OER is quite a complicated process as it involves four proton-coupled electrons transfer, O-H bond breaking and O-O bond formation.^[43] Accordingly, OER has been recognized as the main limitation in the development of water electrolyzers.

Recent researches have shown a promising strategy to overcome this bottleneck by replacing OER with electrochemical oxidation of more favorably oxidized molecules, such as methanol,^[44] ethanol,^[45] glycol,^[46] benzyl alcohol,^[27] urea,^[46-51] 5-hydroxymethylfurfural^[52] and hydrazine,^[53-55] etc. These molecules could be readily oxidized and converted into other chemicals at lower thermodynamic potentials than that of OER (1.23 V vs. reversible hydrogen electrode, RHE) at the anode, thus remarkably decreasing the cell voltage for hydrogen production. Yu et. al synthesized highly porous NiMoO₄ nanorods by annealing treatment in Argon atmosphere, which exhibits an extraordinary catalytic activity for urea oxidation reaction (UOR, $\text{CO}(\text{NH}_2)_2 + 6\text{OH}^- \rightarrow \text{N}_2 + \text{CO}_2 + 5\text{H}_2\text{O} + 6\text{e}^-$, 0.37 V vs. RHE).^[48] The anodic electrode requires just a low potential of 1.37 V vs. RHE at 10 mA cm⁻² in 1 M KOH/0.5 M urea electrolyte. Meanwhile, the urea electrolyzer delivers a small cell voltage of 1.38 V at 10 mA cm⁻². Compared with UOR, hydrazine oxidation reaction (HzOR, $\text{N}_2\text{H}_4 + 4\text{OH}^- \rightarrow \text{N}_2 + 4\text{H}_2\text{O} + 4\text{e}^-$, -0.33 V vs. RHE) possesses an even lower standard potential.^[53, 55] Moreover, this anodic oxidation process only produces nitrogen and water, without any greenhouse gases emission. These advantages indicate that HzOR has a great potential to replace OER for water electrolysis. Accordingly, developing the bifunctional catalysts with high electrocatalytic activity towards both anodic HzOR and cathodic HER is an effective strategy for hydrogen production. As known, a bifunctional catalyst can not only avoid the side reactions induced by different catalysts, but also greatly simplify the catalytic electrode design and construction.^[56-57] Recently, great attentions have been paid to exploring high performance catalysts for HzOR, including noble metal (Pt, Pd),^[58-59] non-noble metal and alloys (Ni, Co, NiCo, NiZn),^[55, 60-61] chalcogenides (NiS₂, CoS₂, CoSe₂)^[53-54, 62] and phosphides (Ni₂P, FeP, Cu₃P).^[63-65] However, fabricating the bifunctional catalytic electrode with superior HER and HzOR activities towards hydrazine-assisted energy-saving hydrogen

production is still a tremendous challenge, needing innovative development of high-performance catalysts. Preparing the bimetal-based catalysts with novel components and architectures by interfacial engineering is a practicable strategy to improve this situation.^[14, 66-69] The interfacial modification approach will expose more active sites, optimize the electronic environment, adjust the catalytic reaction intermediates adsorption and favor the electron and mass transportation. Both theoretical calculations and experimental explorations have indicated that the electrocatalytic performance of bimetal catalysts can be more easily optimized than that of the corresponding individual compounds.^[26-27, 29, 70-72] Chai and co-workers reported a series of promising bimetal catalysts, such as Ni_{0.6}Co_{1.4}P^[70], Ni-Fe-P,^[71] and Fe_{0.125}Ni_{0.875}Se₂^[72] etc., which have been demonstrated for efficient water electrolysis. Lin and co-workers developed a bimetallic copper-cobalt-based phosphide with nitrogen-doped carbon (Cu_{0.3}Co_{2.7}P/NC) as a bifunctional electrocatalyst in alkaline solution.^[21] Cu incorporation could effectively modify the electronic structure and optimize the intermediate adsorption energy to accelerate the catalytic kinetics. The synergistic effects between two different host atoms or components endow the compound with an outstanding catalytic potential. Considering the good metallic conductivity, low electrical resistance and superior corrosion stability, metal nitrides have been paid extensive attention for water electrolysis.^[26-27, 29-31] To the best of our knowledge, copper-nickel-based nitride used as a bifunctional electrocatalyst for HER and HzOR has been rarely reported. Based on these concerns, it could be hypothesized that constructing the bimetallic copper-nickel-based nitride with nickel nitride/copper nitride interface might provide a new approach to achieving exceptional bifunctional electrocatalyst through hydrazine-assistance for energy-saving electrolytic hydrogen production.

Herein, we constructed copper-nickel nitride ($\text{Cu}_1\text{Ni}_2\text{-N}$) porous nanosheets supported on the carbon fiber cloth (CFC), which was prepared using copper-nickel layered double hydroxide (CuNi-LDH) precursor through a thermal ammonolysis process. The three-dimensional (3D) catalyst electrode exhibits both outstanding performance for HER and HzOR. Specifically, $\text{Cu}_1\text{Ni}_2\text{-N}$ electrode shows an overpotential of 71.4 mV at 10 mA cm^{-2} in 1 M KOH, simultaneously delivering an ultralow potential of 0.5 mV at 10 mA cm^{-2} for HzOR in 1.0 M KOH/0.5 M hydrazine electrolyte. Furthermore, when the bifunctional catalyst electrode was utilized as cathode and anode, a water electrolysis system is operated at a cell voltage of a mere 0.24 V to reach the current density of 10 mA cm^{-2} with 75 h durability in the alkaline electrolyte with hydrazine. The exceptional performance can be ascribed to the high electrical conductivity, porous morphology of interconnected nanostructures with large surface area, superhydrophilic electrode surface, synergistic catalytic effects of nickel nitride and copper nitride. Moreover, the hydroxide species, disorder structures and rich defects generated during the catalytic reactions might also contribute to promoting the catalytic activity.

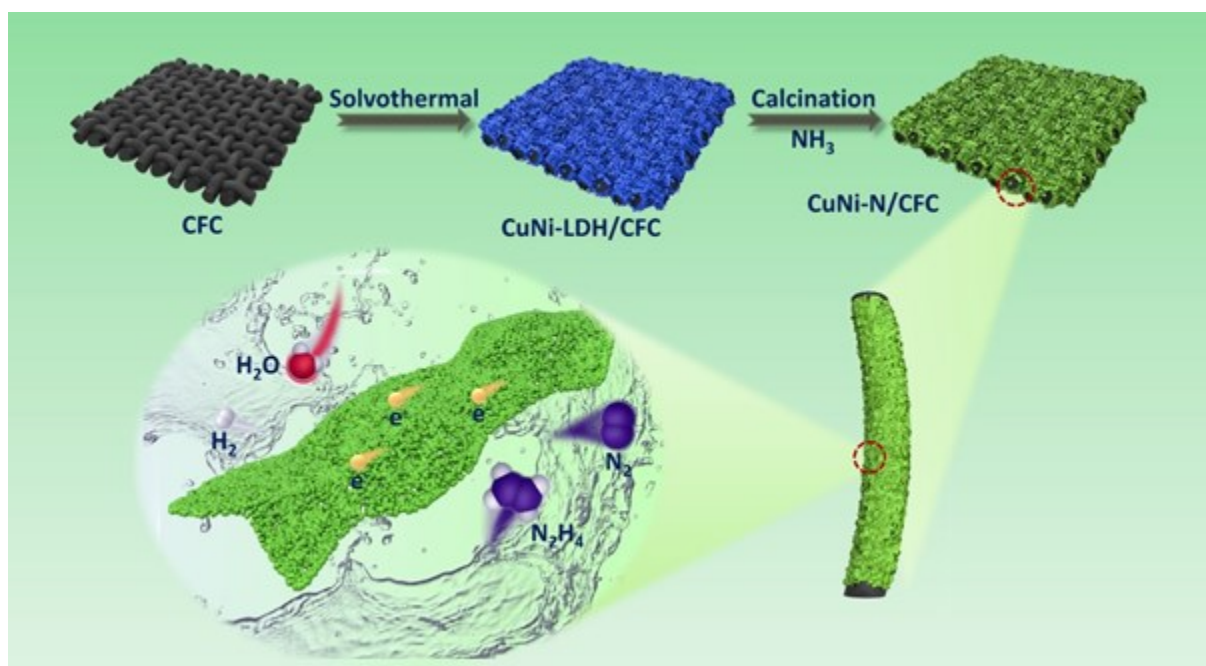


Figure 1. Schematic illustration of the formation process of $\text{Cu}_1\text{Ni}_2\text{-N/CFC}$ electrode.

2. Results and Discussion

As schematically illustrated in Figure 1, $\text{Cu}_1\text{Ni}_2\text{-N}$ nanosheets supported on CFC were prepared through a two-step process and the synthetic details have been described in the Supporting Information. Firstly, the $\text{Cu}_1\text{Ni}_2\text{-LDH}$ nanosheet precursor was synthesized by a facile solvothermal treatment of $\text{Cu}(\text{NO})_2\cdot 3\text{H}_2\text{O}$, $\text{Ni}(\text{NO})_2\cdot 6\text{H}_2\text{O}$ and hexamethylene tetramine (HMT) in methanol at $180\text{ }^\circ\text{C}$ for 12 h.^[73] A subsequent thermal ammonolysis process at $400\text{ }^\circ\text{C}$ for 2 h was undertaken to obtain the $\text{Cu}_1\text{Ni}_2\text{-N}$ electrode. Figure S1A presents the X-ray diffraction (XRD) spectrum of $\text{Cu}_1\text{Ni}_2\text{-}$ based precursor, which exhibits a typical layered structure. The diffraction peaks observed at 10.9° , 21.8° and 33.6° can be assigned to the (003), (006) and (009) planes of hydrotalcite, respectively.^[74]

This article is protected by copyright. All rights reserved.

As shown in the scanning electron microscopy (SEM) images of Figure S1B-C, the $\text{Cu}_1\text{Ni}_2\text{-LDH}$ precursor nanosheets with smooth surface are uniformly wrapped on the CFC. These nanosheets with a thickness of 20~30 nm are in close contact forming a network. Energy-dispersive X-ray (EDX) spectrum displays the existence of Cu and Ni with an atomic ratio of 1:2.4. Similarly, $\text{Ni}(\text{OH})_2 \cdot x\text{H}_2\text{O}$ is confirmed as the Ni-based precursor, which also appears as a layered structure with nanosheet networks morphology (Figure S1D-F). Cu-based precursor was synthesized through a typical hydrothermal method, which could be attributed to $\text{Cu}_2\text{CO}_3(\text{OH})_2$ phase with nanobelt morphology from the XRD pattern and SEM images (Figure S4). After thermal ammonolysis treatment, the hydroxide or subcarbonate precursors were converted into metal nitrides. XRD spectrum of the prepared $\text{Cu}_1\text{Ni}_2\text{-N}$ electrode is shown in Figure 2A. Compared with CFC, for the pattern of $\text{Cu}_1\text{Ni}_2\text{-N}$, the peaks located at 38.5° , 42.3° , 44.3° and 70.8° can be assigned to the (110), (002), (111) and (300) planes of Ni_3N , respectively (JCPDS No. 10-0280) and the peaks at 41.3° and 47.9° matched well with the (111) and (200) planes of Cu_4N , respectively (JCPDS No. 47-1072). As shown in the SEM images (Figure S2A-B, Figure 2B-C), the nanosheets morphology of $\text{Cu}_1\text{Ni}_2\text{-LDH}$ can be well reserved after annealing in NH_3 . Moreover, $\text{Cu}_1\text{Ni}_2\text{-N}$ nanosheets become rough and thinner with a thickness of ~7 nm and a lateral length of ~1.5 μm , which form networks supported on the CFC with a large coverage. Such highly open and interconnected network could promote the accessibility of electrolyte and accelerate the electron transport. The transmission electron microscopy (TEM) images are shown in Figure 2D-E, which verify that the surface of the nanosheet are composed of several nanoparticles with an average size of 6 nm. As comparison, the nanoparticles on the surface of Ni_3N nanosheets are bigger in dimensions with an average size of 21 nm (Figure S3D). In the high-resolution transmission electron microscopy (HRTEM) image of $\text{Cu}_1\text{Ni}_2\text{-N}$ (Figure 2F), the overlapping

lattice fringe with an interplanar spacing of 0.231 nm can be indexed to the (110) crystal planes of Ni₃N, respectively, and the interplanar distance of 0.190 nm can be indexed to the (200) planes of Cu₄N, respectively. Notably, the distorted lattice structure can be observed (labeled by the yellow oval), which is derived by the mismatch of the two nitrides. The distorted lattice arrangement may offer additional active sites for catalytic reactions.^[40] In addition, the high angle annular dark field scanning TEM (HAADF-STEM) and element mapping analysis reveal that the Cu, Ni and N elements are distributed on the whole Cu₁Ni₂-N nanosheet. The corresponding EDX spectrum confirms that the atomic ratio of Cu to Ni is 1:2.3. We compared the electrical conductivity of Cu₁Ni₂-N and Ni-N based on the *I-V* curves (Figure S5). The conductivity of Cu₁Ni₂-N is $8.1 \times 10^3 \text{ S m}^{-1}$, much higher than that of Ni-N ($5.4 \times 10^3 \text{ S m}^{-1}$). Note that the electric conductivity of copper-nickel nitride is superior to that of nickel nitride, which is similar with the previous results of bimetallic catalysts.^[18, 41] The improved conductivity can be attributed to the enhanced carrier density near the Fermi level induced by the strong coupling interactions between nickel nitride and copper nitride.^[26, 28] The surface area and pore size of the Cu₁Ni₂-N nanosheets are determined by N₂ sorption measurements. As shown in Figure S6, the Brunauer–Emmett–Teller (BET) specific surface area is $61.83 \text{ m}^2 \text{ g}^{-1}$ for Cu₁Ni₂-N, which is about two times higher than that for Ni-N ($32.39 \text{ m}^2 \text{ g}^{-1}$). Although Cu₁Ni₂-N and Ni-N exhibit similar pore-size distribution (0-50 nm), Cu₁Ni₂-N displays a much higher pore volume of $0.2 \text{ cm}^3 \text{ g}^{-1}$ than that of Ni-N ($0.05 \text{ cm}^3 \text{ g}^{-1}$). The porous structure and large surface area could provide more active sites, enable more contact area with the electrolyte and contribute towards fast mass transport, which are considered to be beneficial for electrocatalysis.^[18, 27, 41] The contact angle was measured to reveal the accessibility of electrolyte into the Cu₁Ni₂-N electrode. Comparatively, the bare CFC displays a superhydrophobic nature with a contact angle of 143° while the Cu₁Ni₂-N

electrode presents superhydrophilic behavior with a very small contact angle of nearly 0° (Figure S7, movie S1). This result implies that the improved electrolyte wettability ensures the sufficient contact, promoting electrocatalytic reactions.

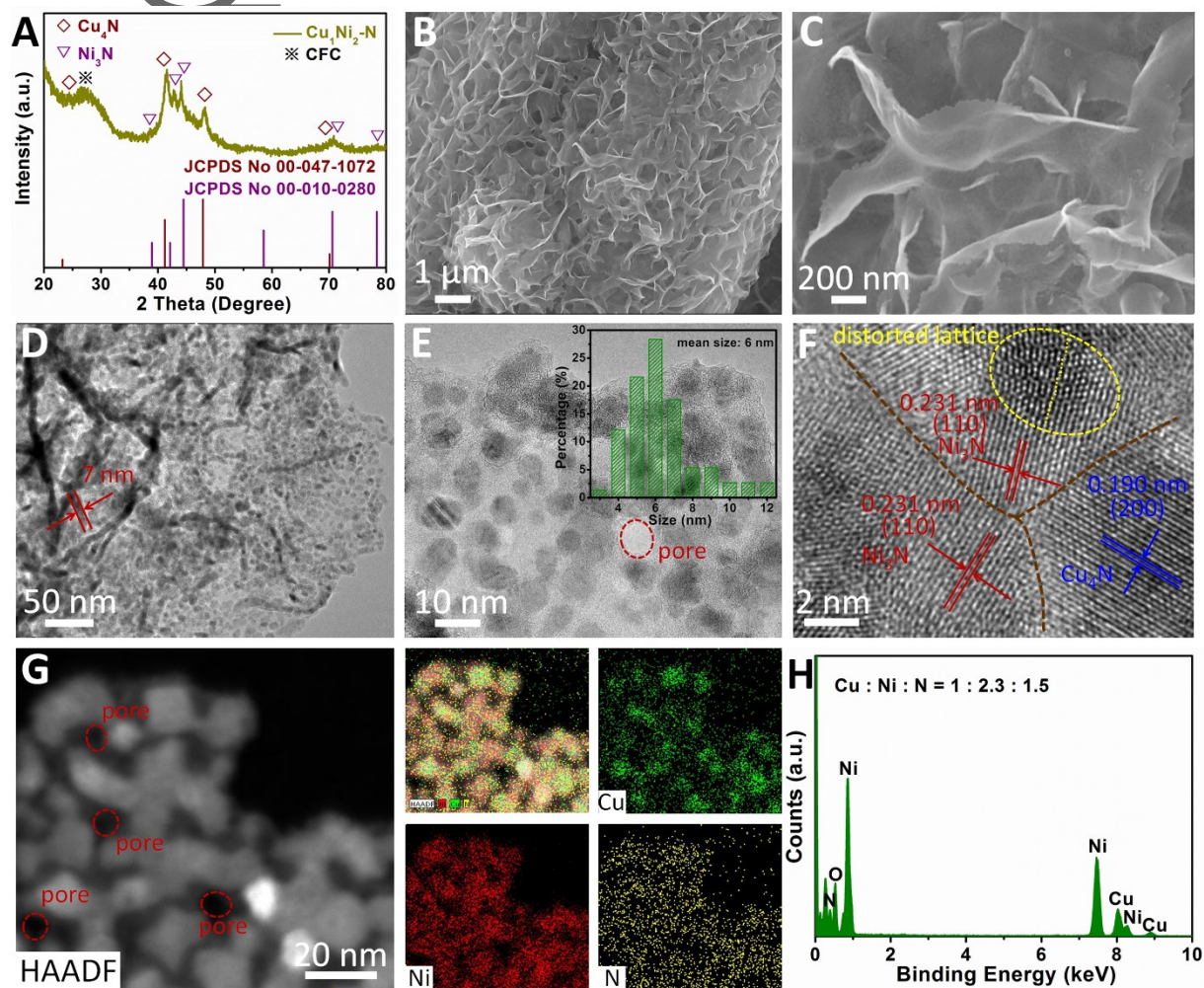


Figure 2. (A) XRD pattern for $\text{Cu}_1\text{Ni}_2\text{-N/CFC}$. (B) Low-magnification and (C) high-magnification SEM images of typical morphology for $\text{Cu}_1\text{Ni}_2\text{-N/CFC}$. (D-E) TEM (inset shows the particle size distribution) and (F) HRTEM images of $\text{Cu}_1\text{Ni}_2\text{-N/CFC}$. (G) HAADF-STEM image and corresponding elemental mapping. (H) The corresponding EDX spectrum.

This article is protected by copyright. All rights reserved.

The surface chemical composition and elemental valence state of the as-prepared $\text{Cu}_1\text{Ni}_2\text{-N}$ and Ni-N were acquired through the X-ray photoelectron spectroscopy (XPS) analysis. As shown in Figure S8, the survey spectrum of $\text{Cu}_1\text{Ni}_2\text{-N}$ reveals the presence of Cu, Ni and N elements, which is consistent with the elemental mapping results. The high-resolution spectrum of Cu 2p can be deconvoluted into four peaks as shown in the Figure 3A. The peaks located at 932.3 and 952.1 eV are ascribed to Cu $2p_{3/2}$ and Cu $2p_{1/2}$, respectively, corresponding to Cu^0/Cu^+ state. Meanwhile, the peaks at 942.7 and 961.9 eV can be attributed to satellite peaks of Cu. The binding energy centered at 934.6 and 954.7 eV are assigned to Cu^{2+} species.⁹³ In Figure 3B, the Ni 2p spectrum of $\text{Cu}_1\text{Ni}_2\text{-N}$ exhibits two main peaks of Ni $2p_{3/2}$ at 852.6 and 855.2 eV with a satellite peak at 861.4 eV, which are related to Ni^0 and Ni^{2+} and the satellite peak. The Ni^0 state indicates a metallic feature of $\text{Cu}_1\text{Ni}_2\text{-N}$, which is consistent with previous reports.^[26, 28] Compared to the Ni $2p_{3/2}$ region of Ni-N, the binding energy exhibits a negative shift of about 0.5 eV. The N 1s spectrum of $\text{Cu}_1\text{Ni}_2\text{-N}$ can be deconvoluted into two peaks. The peak located at 398.5 eV is assigned to N–Ni/Cu bonds, which further confirms the formation of the nitride. Another peak at 399.2 eV is ascribed to N–H bonds, which indicates the presence of a number of H species on the catalyst surface. Similarly, in comparison with N 1s spectrum of Ni-N, the binding energy of N–metal displays a negative shift of about 0.3 eV. XPS results suggest the existence of strong electronic interactions between Ni_3N and Cu_4N , which may induce the redistribution of charge on the coupling interfaces.^[15, 49, 75-76]

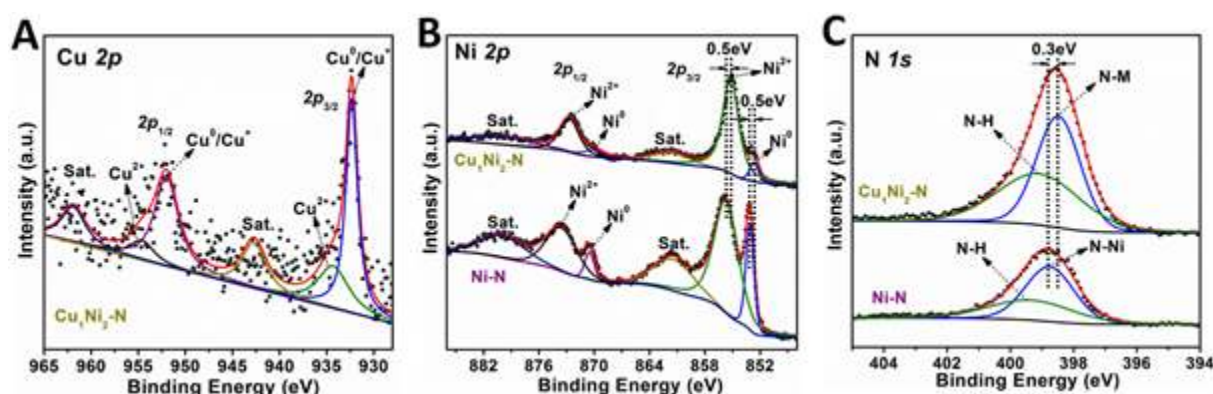


Figure 3. High-resolution XPS spectra. (A) Cu 2p spectra of Cu₁Ni₂-N. (B) Ni 2p and (C) N 1s spectra of Cu₁Ni₂-N and Ni-N.

To evaluate the electrocatalytic performance for HER, Cu₁Ni₂-N electrode was tested in 1.0 M KOH solution using a typical three-electrode configuration. For comparison, bare CFC, Ni-N, Cu-N, Cu₁Ni₂-LDH, Ni(OH)₂, Cu-pre, commercial Pt/C and IrO₂ supported on CFC were also evaluated as control experiments. The linear sweep voltammetry (LSV) curves of the different samples were corrected for iR compensation. As shown in Figure 4A and Figure S12A, the onset potential of Cu₁Ni₂-N electrode is much smaller at around 18 mV when compared with Ni-N (113 mV), Cu-N (214 mV), Cu₁Ni₂-LDH (367 mV), Ni(OH)₂ (443 mV) and Cu-pre (273 mV), respectively. Additionally, at a current density of 10 mA cm⁻², the Cu₁Ni₂-N electrode exhibits the lowest overpotential of 71.4 mV, compared with Ni-N (185.6 mV), Cu-N (317 mV), Cu₁Ni₂-LDH (431.6 mV), Ni(OH)₂ (483.9 mV) and Cu-pre (398 mV). The Cu₁Ni₂-N displays exceptional superior catalytic activity for HER over the other recently reported highly efficient noble metal-free catalysts, such as Ni-doped FeP (95 mV),^[22] Ni₃FeN/r-GO (94 mV),^[26] NC@CuCoN_x (105 mV),^[27] (Co_{1-x}Ni_x)(S_{1-y}P_y)₂/G (117 mV),^[77] NG-NiFe@MoC₂ (150 mV),^[78] et. al as

listed in Table S1. In Figure S9, the catalyst prepared at a calcination temperature of 400 °C and a Cu/Ni molar ratio of 1:2 presents a greater activity for HER. By fitting the LSV curves of the catalysts, the corresponding Tafel plots can be obtained to evaluate the HER kinetics. Figure 4C and Figure S12B show that the Tafel slope of Cu₁Ni₂-N is 106.5 mV dec⁻¹, which is substantially lower than Ni-N (149.1 mV dec⁻¹), Cu-N (151.9 mV dec⁻¹), Cu₁Ni₂-LDH (304.2 mV dec⁻¹), Ni(OH)₂ (390.1 mV dec⁻¹) and Cu-pre (167.2 mV dec⁻¹). This means that the Cu₁Ni₂-N electrode shows an enhanced HER kinetics. To further understand the intrinsic activity of different catalysts, the double layer capacitance (C_{dl}) is evaluated to measure the electrochemically active surface area (ECSA). As illustrated in Figure 4D and Figure S10, derived from the cyclic voltammograms (CV) at different scan rates, the ECSA of Cu₁Ni₂-N, Ni-N, Cu-N, Cu₁Ni₂-LDH, Ni(OH)₂, Cu-pre and CFC was calculated to be 42.02, 13.18, 14.01, 2.72, 2.06, 7.19 and 1.57 mF cm⁻², respectively. Meanwhile, the roughness factors (RFs) of the samples were calculated (Figure S10H). In contrast, the Cu₁Ni₂-N electrode exhibits the highest active surface area and RF, which can be mainly attributed to the porous nanosheet structure and large surface area. The ECSA-normalized LSV curves in Figure 4E and Figure S12D is utilized to highlight the intrinsic catalytic activity. It is obvious that the ECSA-normalized current density of Cu₁Ni₂-N is larger than that of Ni-N, Cu-N, Cu₁Ni₂-LDH, Ni(OH)₂ and Cu-pre at -0.2 V vs. RHE, suggesting that the higher HER activity of Cu₁Ni₂-N results from not only the increased ECSA but also the enhanced intrinsic catalytic activity induced by the Ni₃N/Cu₄N interface. The turn over frequency (TOF) per surface site of catalysts were calculated to further evaluate intrinsic catalytic activities. The amount of active sites were quantified from the CV plots tested in phosphate buffered solution.^[19] Compared with nickel nitride, the bimetallic copper-nickel nitride provides more active sites (Figure S11). The calculated TOF value of Cu₁Ni₂-N is 0.49 s⁻¹ at the overpotential of 150 mV in Figure 4F, which is

higher than those of Ni-N (0.08 s^{-1}), Cu-N (0.02 s^{-1}), $\text{Cu}_1\text{Ni}_2\text{-LDH}$ (0.05 s^{-1}), Ni(OH)_2 (0.02 s^{-1}) and Cu-pre (0.01 s^{-1}). The tendency of TOF values is in full agreement with the intrinsic catalytic activity for HER, suggesting that the greatly enhanced HER activity of $\text{Cu}_1\text{Ni}_2\text{-N}$ is mainly benefited from the synergistic catalytic effects induced by the intrinsic constructed interfaces between nickel nitride and copper nitride. Electrochemical impedance spectroscopy (EIS) measurements were conducted to investigate the electrode kinetics during the HER process. As shown in Figure 4G and Figure S12F, the Nyquist plots indicate that the $\text{Cu}_1\text{Ni}_2\text{-N}$ electrode possesses the smallest charge transfer resistance (R_{ct}) among all the samples, revealing a faster charge transfer and more favorable reaction kinetics for HER catalysis. Besides the catalytic activity, the durability of catalyst is also an important and challenging factor for practical applications. The long-term electrochemical stability at a current density of 10 mA cm^{-2} were tested by a chronoamperometry measurement with a negligible deactivation over 60 h (Figure 4H), confirming the excellent stability of $\text{Cu}_1\text{Ni}_2\text{-N}$ towards HER.

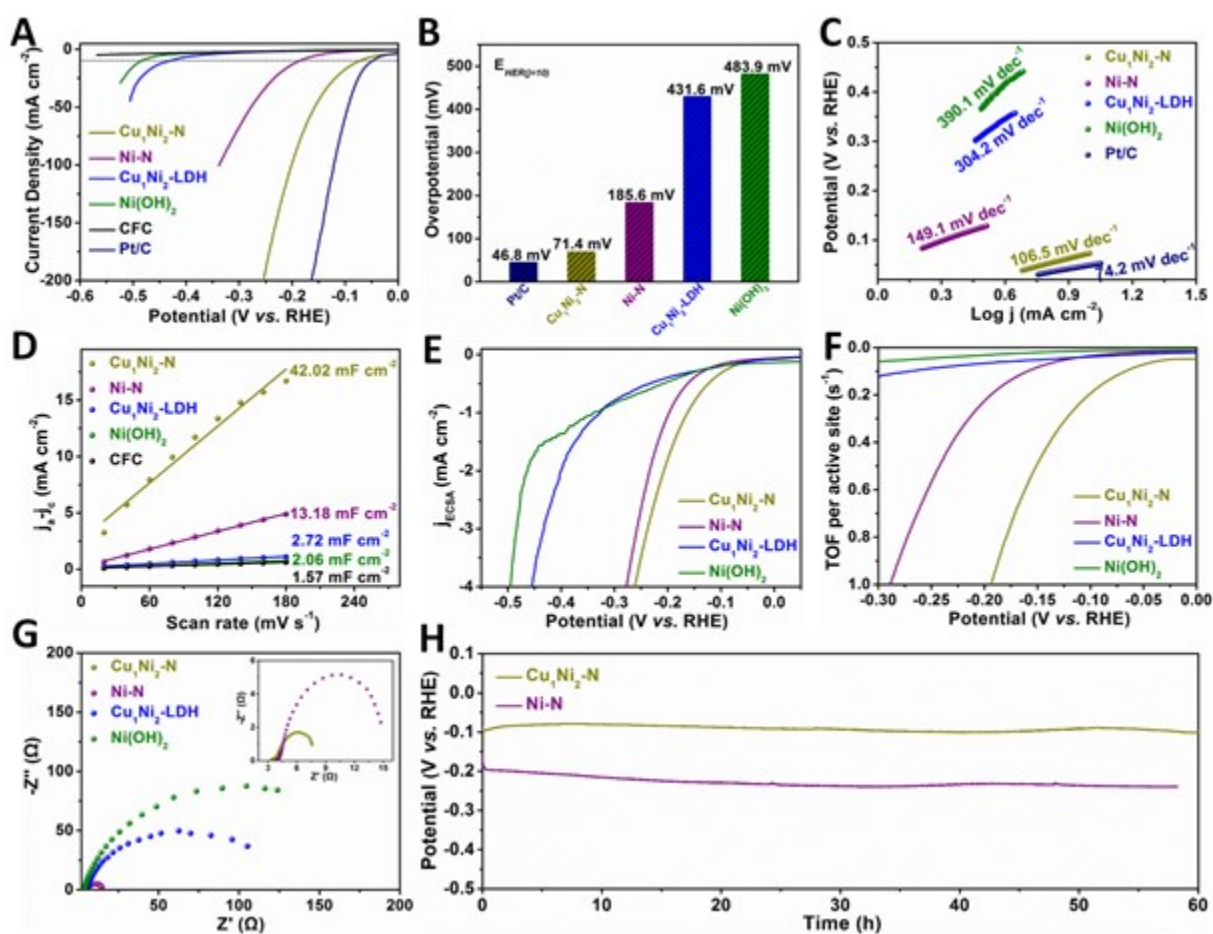


Figure 4. Electrochemical performance of electrodes for the HER measured in 1.0 M KOH solution. (A) Polarization curves for Cu₁Ni₂-N, Ni-N, Cu₁Ni₂-LDH, Ni(OH)₂, Pt/C and CFC at a scan rate of 5 mV s⁻¹. (B) The overpotentials required for $j = 10 \text{ mA cm}^{-2}$ with different samples. (C) The corresponding Tafel plots. (D) Estimation of C_{dl} by plotting the current density at 0.124 V vs. RHE. (E) Polarization curves of different samples normalized by the electrochemical active surface area (ECSA). (F) The turnover frequencies (TOFs) at different potentials. (G) Electrochemical impedance spectroscopy for the corresponding electrocatalysts. (H) Long-time stability test of the of Cu₁Ni₂-N and Ni-N at constant current densities of 10 mA cm⁻².

This article is protected by copyright. All rights reserved.

We further investigated the OER performance of the Cu₁Ni₂-N electrode in 1 M KOH solution. It can deliver a current density of 20 mA cm⁻² at low overpotential of 312 mV. For comparison, Ni-N, Cu-N and IrO₂ require overpotential of 405, 498 and 324 mV to deliver the same current density, respectively (Figure S13). Considering the undesirable overpotential of Cu₁Ni₂-N for OER (312 mV at 20 mA cm⁻²), it will require much higher electrical energy to be utilized as the anode for water splitting. In contrast, HzOR provides an ideal anodic alternative due to its extremely low thermodynamic voltage of -0.33 V vs. RHE.^[53, 55] Therefore, the cell voltage of water electrolysis can be greatly decreased by replacing the sluggish OER with the thermodynamically more favorable HzOR. We investigated the HzOR activities of samples in a three-electrode system at a scan rate of 5 mV s⁻¹ in alkaline electrolyte. Figure 5A shows the LSV curves of Cu₁Ni₂-N electrode in 1.0 M KOH with different concentrations of hydrazine. It is obvious that no anodic current density is observed in the potential window of -0.1~0.5 V vs. RHE when tested without hydrazine. In contrast, the addition of 0.1 M hydrazine solution results in a noticeable promotion in anodic current density. Meanwhile, the response current density rises along with the increasing concentration of hydrazine solution from 0.1~0.5 M. At high concentrations, such as 1 M and 2 M hydrazine solution (Figure S16A), the corresponding LSV curves are generally the same. Figure 5B and Figure S17 presents the electrocatalytic HzOR activity of Cu₁Ni₂-N, Ni-N, Cu-N, Cu₁Ni₂-LDH, Ni(OH)₂, Cu-pre and Pt/C electrodes measured in 1 M KOH/0.5 M hydrazine electrolyte. Both Cu₁Ni₂-LDH and Ni(OH)₂ samples display negligible anodic current density. The Cu₁Ni₂-N electrode possesses superior HzOR activity and can deliver anodic current density of 10 mA cm⁻² and 50 mA cm⁻² at 0.5 and 96.9 mV, respectively, indicating a more negative value than those of Ni-N, Cu-N and Pt/C electrodes. We also

This article is protected by copyright. All rights reserved.

investigated the performance of electrodes with different Cu/Ni molar ratios (Figure S16B). It is obvious that the catalyst with a Cu/Ni molar ratio of 1:2 exhibits the highest activity for HzOR. As displayed in Figure 5C and Figure S17B, the Tafel slope of Cu₁Ni₂-N electrode (44.1 mV dec⁻¹) is much smaller than that of Ni-N (110.3 mV dec⁻¹), Cu-N (62.9 mV dec⁻¹) and Pt/C (72.5 mV dec⁻¹), which suggests that it has more favorable catalytic kinetics for HzOR. There are no apparent changes in the LSV curves at the different scan rates from 5 to 50 mV s⁻¹, revealing the efficient charge and mass transport in HzOR catalytic process.^[47, 63] As presented in Figure 5E, the Cu₁Ni₂-N electrode shows an outstanding long-term stability when tested at a constant current density of 10 mA cm⁻² for 35 h with insignificant potential decay.

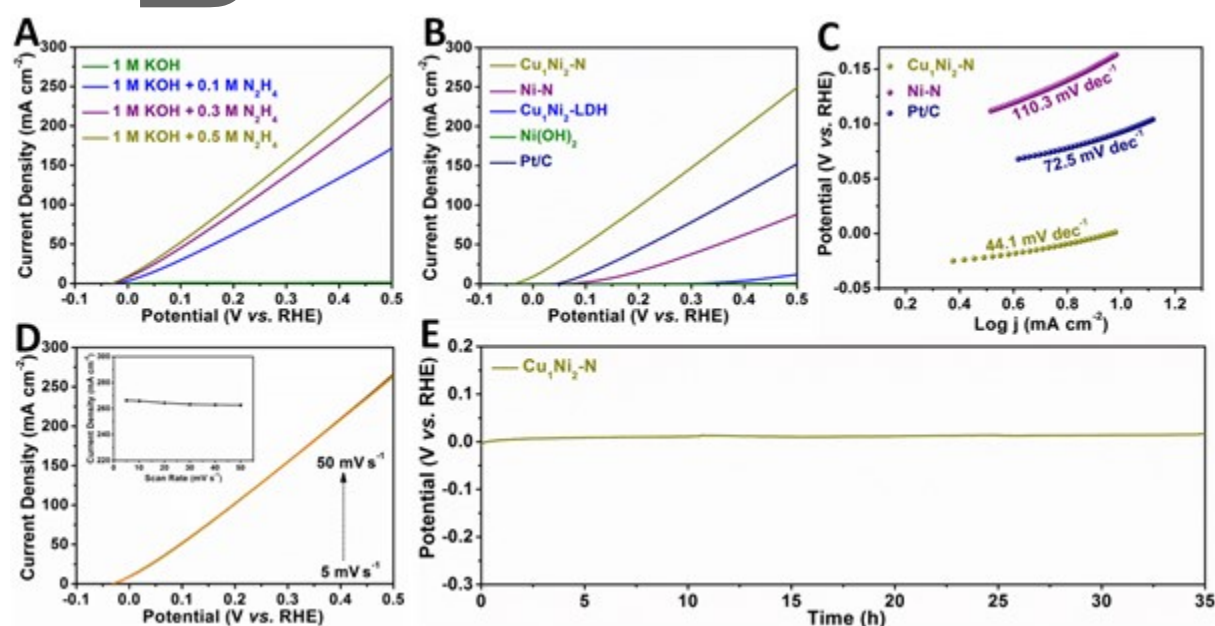


Figure 5. Electrochemical performance of electrodes for the HzOR. (A) Polarization curves of Cu₁Ni₂-N toward different concentrations of hydrazine. (B) Polarization curves of Cu₁Ni₂-N, Ni-N, Cu₁Ni₂-LDH, Ni(OH)₂ and Pt/C in 1.0 M KOH/0.5 M hydrazine electrolyte. (C) The corresponding Tafel plots. (D) Polarization curves of Cu₁Ni₂-N toward 0.5 M hydrazine at different scan rates (inset: the

This article is protected by copyright. All rights reserved.

corresponding current density at 0.5 V for different scan rates). (E) Long-time stability test of the of $\text{Cu}_1\text{Ni}_2\text{-N}$ at a constant current density of 10 mA cm^{-2} .

To get further insight of the catalytic reaction, the morphology, structural and chemical states of $\text{Cu}_1\text{Ni}_2\text{-N}$ electrode were investigated after HER and HzOR. In the Figure S19A-C, the nanosheet morphology of the $\text{Cu}_1\text{Ni}_2\text{-N}$ is retained well after long-term HER measurement as evidenced by SEM images. The porous structure and nanoparticles could be also viewed from TEM and HAADF-STEM images (Figure S19D, G). In the HRTEM image (Figure S19E), the lattice fringe spacings of 0.214 and 0.219 nm are well indexed to the (002) plane of Ni_3N and (111) plane of Cu_4N , respectively. This result confirms that the major nitride phases could be maintained during electrolysis. However, Figure S19F displays the lattice fringe spacings of 0.236 nm, which could be attributed to the (101) plane of $\text{Ni}(\text{OH})_2$. The element mapping shows the distribution of Cu, Ni, N and O in the nanosheet. Furthermore, three small diffraction peaks at 33.1° , 38.5° and 59.2° could be assigned to the (100), (101) and (110) planes of $\text{Ni}(\text{OH})_2$ in the XRD pattern after HER (Figure 6D). XPS analysis was further studied to verify the transformation on the surface of the catalyst after HER. In comparison with the XPS spectrum of original $\text{Cu}_1\text{Ni}_2\text{-N}$, the peak intensities of low-valent Cu (932.3 eV) and Ni (852.6 eV) decrease, while the peak intensities of high-valent Cu (935.1 eV) and Ni (855.2 eV) increase after HER measurement (Figure 6A-B). Moreover, the N signal still could be detected in Figure 6C. These observations indicate that $\text{Ni}(\text{OH})_2$ was generated on the surface of the $\text{Cu}_1\text{Ni}_2\text{-N}$ after HER catalysis. Similar results could be also obtained after HzOR (Figure 6A-B, S20). This observation might be attributed to the thermodynamic instability of the nitride surface during

the electrocatalytic reactions. This kind of hydroxylated phenomenon during electrolysis have also been reported in the previous works.^[18, 77, 79] The hydroxide species produced from nitrides during electrolysis probably offer the favorable active sites for hydroxyl adsorption.^[16, 67, 80] Meanwhile, the remaining nitrides provide the active sites for intermediates adsorption and support the efficient transport of electrons. Recently, the Ni-based hydroxides in the composite catalysts are able to act as the water dissociation promoter and hydroxyl acceptor, which could favor the absorption of H₂O and optimize catalyst-intermediate energetics to accelerate the catalytic kinetics.^[16, 67] Besides, disorder structures and rich defects could be created during the process of electrolysis (Figure S19E-F, S20E-F), which could promote the catalytic activity.^[81-82]

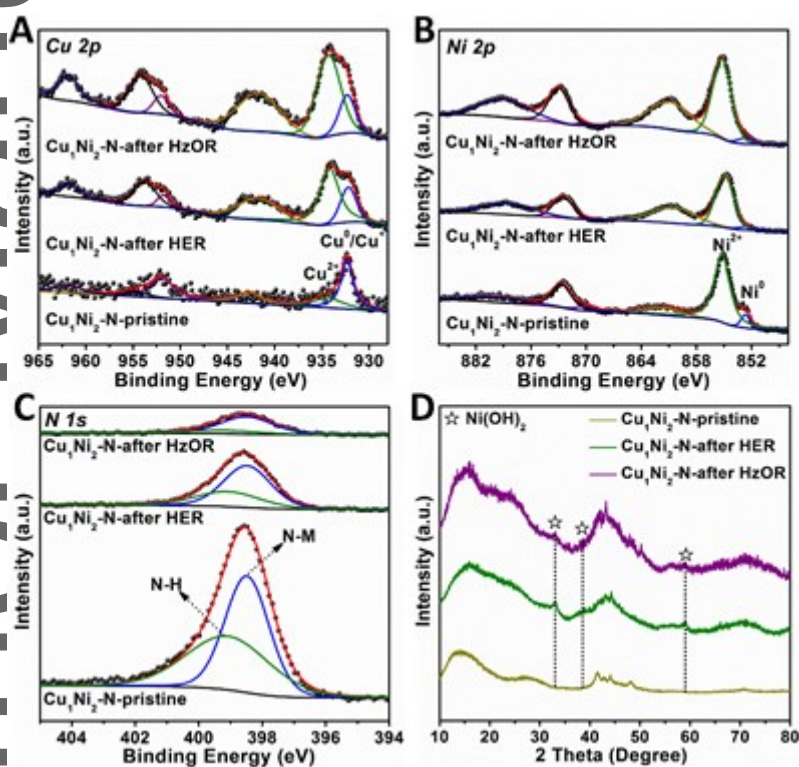


Figure 6. XPS and XRD characterization after HER and HzOR test. (A) Cu 2p, (B) Ni 2p, (C) N 1s spectra, and (D) XRD patterns of Cu₁Ni₂-N before and after HER and HzOR tests.

This article is protected by copyright. All rights reserved.

As shown in Figure S16D, the LSV curves of Cu₁Ni₂-N electrode for HER only presents a small positive shift of 13 mV in 1.0 M KOH/0.5 M hydrazine electrolyte, indicating that excellent HER activity can be retained with the presence of hydrazine. Inspired by the superior HzOR and HER catalytic performance of the Cu₁Ni₂-N electrode (Figure 7C), we assembled a two-electrode cell employing the Cu₁Ni₂-N electrode as both anode and cathode for water electrolysis as schematically presented in Figure 7A. Besides, the two-electrode system integrated with OER and HER was also measured in 1 M KOH electrolyte for comparison. Digital photograph of the two-electrode configuration towards hydrazine-assisted hydrogen generation during operation is shown in Figure 7B. For water splitting, the two-electrode systems utilizing Cu₁Ni₂-N and Ni-N electrode require much larger voltage of 1.63 and 1.82 V, respectively to reach the 10 mA cm⁻² in 1 M KOH solution, while the hydrazine-assisted electrolysis system assembled with Cu₁Ni₂-N electrode delivers a cell voltage of only 0.24 V. Additionally, it presents a robust stability with a negligible deactivation over 75 h in Figure 7E. Comparing with the recently reported state-of-the-art bifunctional catalysts, Cu₁Ni₂-N electrode exhibits a superior activity for water electrolysis (Table S2). Vigorous gas bubbles can be clearly observed on the individual electrode surfaces (Movie S2, Supporting Information). The amount of hydrogen generated from the cathode was collected by a drainage system during electrolysis. As shown in Figure S18, the agreement of the amount of hydrogen gas determined by experimentally and theoretical suggests a Faradaic efficiency of nearly 95%.

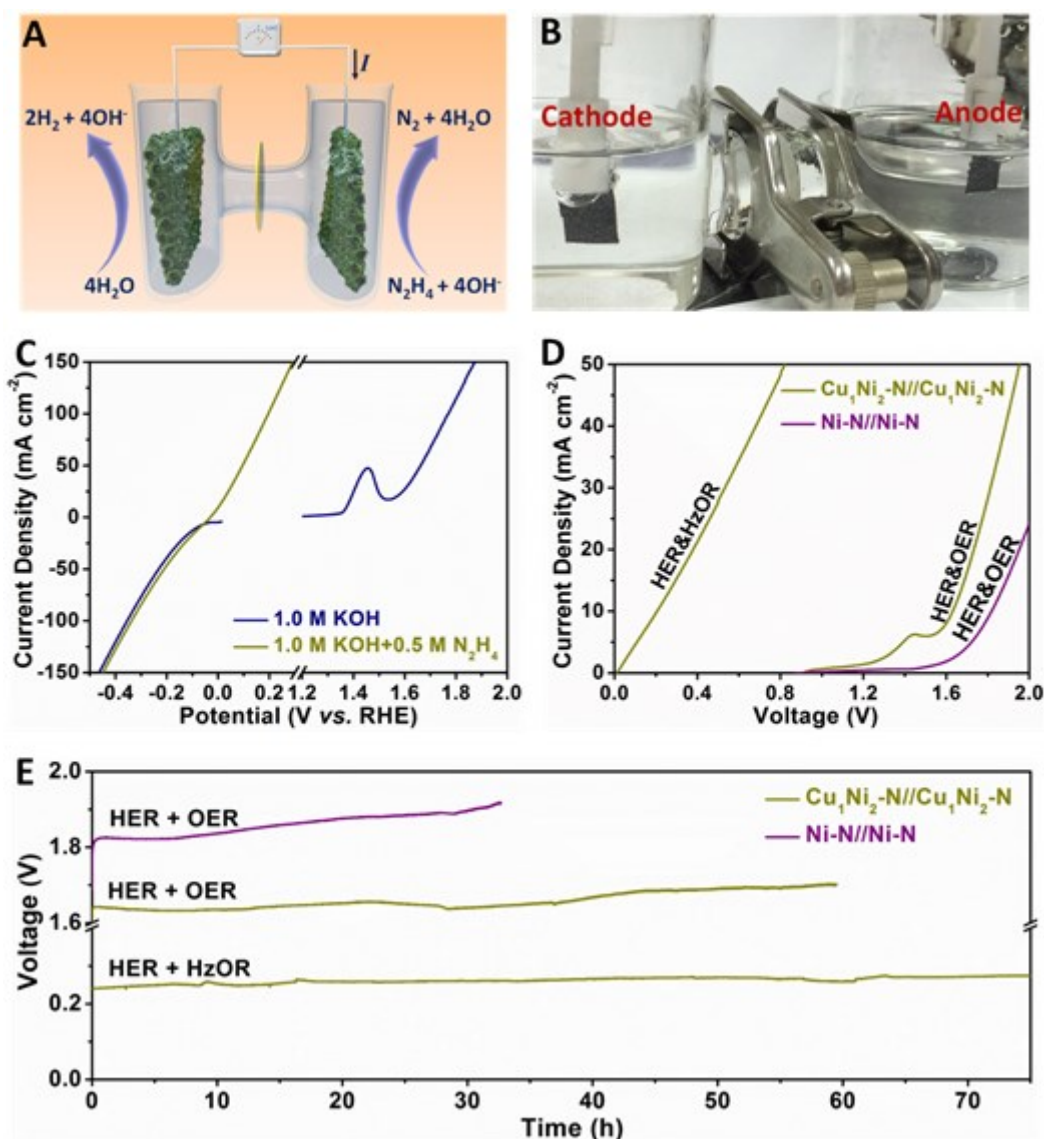


Figure 7. Performance of hydrazine-assisted water electrolysis for hydrogen production. (A) The schematic illustration of two-electrode cell using $\text{Cu}_1\text{Ni}_2\text{-N}$ electrode as both anode and cathode for hydrazine-assisted water electrolysis. (B) Digital photograph of the two-electrode configuration. (C) Polarization curves of $\text{Cu}_1\text{Ni}_2\text{-N}$ for HER, OER and HzOR without iR -corrected. (D) Comparison of polarization curves for water electrolysis with and without hydrazine at a scan rate of 5 mV s^{-1} . (E)

This article is protected by copyright. All rights reserved.

Long-time stability tests of water electrolysis with and without hydrazine at constant current density of 10 mA cm^{-2} .

Density functional theory (DFT) calculations were performed to gain insight into the outstanding catalytic activity of $\text{Cu}_1\text{Ni}_2\text{-N}$ with $\text{Cu}_4\text{N}/\text{Ni}_3\text{N}$ interface. Figure S21 exhibits the schematic models, total and partial electronic density of states for $\text{Cu}_4\text{N-Ni}_3\text{N}$, Cu_4N and Ni_3N .

It is clear that the three kinds of metal nitrides have no band gap in the band structure, which indicates the metallic nature. Meanwhile, electron occupied states near the Fermi level on $\text{Cu}_4\text{N-Ni}_3\text{N}$ are much higher than those of Cu_4N and Ni_3N , revealing higher electrical conductivity and stronger carrier density. Notably, the d-band center of $\text{Cu}_4\text{N-Ni}_3\text{N}$ (-2.24 eV) is downshifted from the Fermi level in comparison with Ni_3N (-1.61 eV), which might decrease the chemical adsorption capability. According to the previous studies,^[13, 83-86] the downward shift of d-band center basically lowers the energy of antibonding states below the Fermi level, leading to favorable adsorption of intermediates and thus high catalytic activity. On the basis of DFT calculations, it indicates that constructing $\text{Cu}_4\text{N}/\text{Ni}_3\text{N}$ interface leads to a positive effect on the electronic characteristics compared with individual nitrides. $\text{Cu}_1\text{Ni}_2\text{-N}$ with $\text{Cu}_4\text{N}/\text{Ni}_3\text{N}$ interface possesses excellent electrical conductivity and fast charge transfer kinetic, which is beneficial to the catalytic reactions.

The superior catalytic activity of $\text{Cu}_1\text{Ni}_2\text{-N}$ electrode could be ascribed to the following advantages. (i) The porous nanosheet morphology assembled by nanoparticles provides large specific surface area with more catalytic active sites, simultaneously enhancing the transfer of electrolyte ion. (ii) 3D catalyst electrode with highly open networks exhibits superhydrophilic behavior, facilitating the penetration of electrolyte and release of gas for electrolysis.^[18] (iii) As confirmed by experiments and

DFT calculations, $\text{Cu}_1\text{Ni}_2\text{-N}$ possesses good electric conductivity which is favorable for fast electron transport in the electrocatalytic reactions. (iv) DOS reveals that the d-band center is downshifted from the Fermi level after Cu_4N incorporation, which decreases the binding strength of H. The strongly coupled interactions between Ni_3N and Cu_4N probably induces the redistribution of charge on the interfaces. This would adjust the electronic structure of materials surface and optimize the adsorption energy of reaction intermediates in the catalytic reactions, synergistically promoting the intrinsic activity.^[15, 49, 75, 87] (v) The hydroxide species generated from nitrides after the catalytic reactions probably offer the favorable active sites for hydroxyl adsorption to accelerate the catalytic kinetics.^[16, 67] (vi) Disorder structures and rich defects created during the electrolysis process could provide strong support for the high catalytic activity.^[81-82] All these advantages greatly contribute to the high performance of $\text{Cu}_1\text{Ni}_2\text{-N}$ electrode and enable it to be a promising alternative for energy-saving hydrogen production.

3. Conclusions

In summary, a class of copper-nickel-based nitride has been successfully constructed on the 3D substrate with rational design for efficient hydrogen generation in the alkaline electrolyte with hydrazine. Benefiting from the high electrical conductivity, porous morphology of interconnected nanostructures with large surface area, superhydrophilic electrode surface, synergistic catalytic effects of nickel nitride and copper nitride, hydroxide species and disorder structures generated during the catalytic reactions, the prepared electrode presents exceptional catalytic performance and greatly stability for HER and HzOR, respectively. A two-electrode water electrolysis system assembled with the $\text{Cu}_1\text{Ni}_2\text{-N}$ electrode as both cathode and anode delivers a small cell voltage of

0.24 V at a current density of 10 mA cm^{-2} over 75 h in 1 M KOH/0.5 M hydrazine electrolyte. This work provides new insights for designing and constructing the low-cost and high activity transition metal bifunctional catalytic electrode for energy-saving hydrogen production.

Supporting Information

Supporting Information is available from the Wiley Online Library or from the author.

Acknowledgements

This work was supported by the National Natural Science Fund for Distinguished Young Scholars (51425204), the National Natural Science Foundation of China (21673171, 51502226, 51802239), the National Key Research and Development Program of China (2016YFA0202603, 2018FYB0104202), the Program of Introducing Talents of Discipline to Universities (B17034), the Fundamental Research Funds for the Central Universities (WUT: 2018IVA091). We are very grateful to Prof. Yan Zhao and Dr. Yalong Jiang for their generous assistance with the DFT calculations.

Conflict of Interest

The authors declare no conflict of interest.

References

- [1] J. A. Turner, *Science* **2004**, 305, 972.
- [2] S. Chu, Y. Cui, N. Liu, *Nat. Mater.* **2017**, 16, 16.
- [3] T. E. Mallouk, *Nat. Chem.* **2013**, 5, 362.
- [4] M. Dresselhaus, I. Thomas, *Nature* **2001**, 414, 332.
- [5] B. You, Y. Sun, *Acc. Chem. Res.* **2018**, 51, 1571.
- [6] I. Roger, M. A. Shipman, M. D. Symes, *Nat. Rev. Chem.* **2017**, 1, 0003.
- [7] Y. Shi, B. Zhang, *Chem. Soc. Rev.* **2016**, 45, 1529.
- [8] N. Cheng, S. Stambula, D. Wang, M. N. Banis, J. Liu, A. Riese, B. Xiao, R. Li, T.-K. Sham, L.-M. Liu, G. A. Botton, X. Sun, *Nat. Commun.* **2016**, 7, 13638.
- [9] C. C. McCrory, S. Jung, J. C. Peters, T. F. Jaramillo, *J. Am. Chem. Soc.* **2013**, 135, 16977.
- [10] Y. Lee, J. Suntivich, K. J. May, E. E. Perry, S.-H. Yang, *J. Phys. Chem. Lett.* **2012**, 3, 399.

This article is protected by copyright. All rights reserved.

- [11] Y. Shen, Y. Zhou, D. Wang, X. Wu, J. Li, J. Xi, *Adv. Energy Mater.* **2018**, 8, 1701759.
- [12] J. Zhang, T. Wang, P. Liu, Z. Liao, S. Liu, X. Zhuang, M. Chen, E. Zschech, X. Feng, *Nat. Commun.* **2017**, 8, 15437.
- [13] Y. Wu, X. Liu, D. Han, X. Song, L. Shi, Y. Song, S. Niu, Y. Xie, J. Cai, S. Wu, J. Kang, J. Zhou, Z. Chen, X. Zheng, X. Xiao, G. Wang, *Nat. Commun.* **2018**, 9, 4531.
- [14] J. Hou, B. Zhang, Z. Li, S. Cao, Y. Sun, Y. Wu, Z. Gao, L. Sun, *ACS Catal.* **2018**, 8, 4612.
- [15] J. Zhang, T. Wang, D. Pohl, B. Rellinghaus, R. Dong, S. Liu, X. Zhuang, X. Feng, *Angew. Chem.* **2016**, 128, 6814.
- [16] J. Hu, C. Zhang, L. Jiang, H. Lin, Y. An, D. Zhou, M. K. Leung, S. Yang, *Joule* **2017**, 1, 383.
- [17] L. Fang, W. Li, Y. Guan, Y. Feng, H. Zhang, S. Wang, Y. Wang, *Adv. Funct. Mater.* **2017**, 27, 1701008.
- [18] H. Liang, A. N. Gandi, D. H. Anjum, X. Wang, U. Schwingenschlögl, H. N. Alshareef, *Nano Lett.* **2016**, 16, 7718.
- [19] F. Yu, H. Zhou, Y. Huang, J. Sun, F. Qin, J. Bao, W. A. Goddard III, S. Chen, Z. Ren, *Nat. Commun.* **2018**, 9, 2551.
- [20] H. Zhang, X. Li, A. Hähnel, V. Naumann, C. Lin, S. Azimi, S. L. Schweizer, A. W. Maijenburg, R. B. Wehrspohn, *Adv. Funct. Mater.* **2018**, 28, 1706847.
- [21] J. Song, C. Zhu, B. Z. Xu, S. Fu, M. H. Engelhard, R. Ye, D. Du, S. P. Beckman, Y. Lin, *Adv. Energy Mater.* **2017**, 7, 1601555.
- [22] X. F. Lu, L. Yu, X. W. D. Lou, *Sci. Adv.* **2019**, 5, eaav6009.
- [23] J. Jia, T. Xiong, L. Zhao, F. Wang, H. Liu, R. Hu, J. Zhou, W. Zhou, S. Chen, *ACS Nano* **2017**, 11, 12509.
- [24] Y. Huang, J. Hu, H. Xu, W. Bian, J. Ge, D. Zang, D. Cheng, Y. Lv, C. Zhang, J. Gu, Y. Wei, *Adv. Energy Mater.* **2018**, 1800789.
- [25] H. Yan, Y. Xie, Y. Jiao, A. Wu, C. Tian, X. Zhang, L. Wang, H. Fu, *Adv. Mater.* **2018**, 30, 1704156.
- [26] Y. Gu, S. Chen, J. Ren, Y. A. Jia, C. Chen, S. Komarneni, D. Yang, X. Yao, *ACS Nano* **2018**, 12, 245.
- [27] J. Zheng, X. Chen, X. Zhong, S. Li, T. Liu, G. Zhuang, X. Li, S. Deng, D. Mei, J. G. Wang, *Adv. Funct. Mater.* **2017**, 27, 1704169.
- [28] A. Wu, Y. Xie, H. Ma, C. Tian, Y. Gu, H. Yan, X. Zhang, G. Yang, H. Fu, *Nano Energy* **2018**, 44, 353.
- [29] J. Hou, Y. Sun, Z. Li, B. Zhang, S. Cao, Y. Wu, Z. Gao, L. Sun, *Adv. Funct. Mater.* **2018**, 28, 1803278.

- [30] H. Jin, X. Liu, A. Vasileff, Y. Jiao, Y. Zhao, Y. Zheng, S. Z. Qiao, *ACS Nano* **2018**, *12*, 12761.
- [31] Y. Ma, Z. He, Z. Wu, B. Zhang, Y. Zhang, S. Ding, C. Xiao, *J. Mater. Chem. A* **2017**, *5*, 24850.
- [32] Z. Li, W. Niu, L. Zhou, Y. Yang, *ACS Energy Lett.* **2018**, *3*, 892.
- [33] P. Zhang, L. Li, D. Nordlund, H. Chen, L. Fan, B. Zhang, X. Sheng, Q. Daniel, L. Sun, *Nat. Commun.* **2018**, *9*, 381.
- [34] L. Yu, H. Zhou, J. Sun, F. Qin, F. Yu, J. Bao, Y. Yu, S. Chen, Z. Ren, *Energy Environ. Sci.* **2017**, *10*, 1820.
- [35] S. H. Ye, Z. X. Shi, J. X. Feng, Y. X. Tong, G. R. Li, *Angew. Chem. Int. Ed.* **2018**, *57*, 2672.
- [36] H. Zhou, F. Yu, Q. Zhu, J. Sun, F. Qin, L. Yu, J. Bao, Y. Yu, S. Chen, Z. Ren, *Energy Environ. Sci.* **2018**, *11*, 2858.
- [37] W. Li, X. Gao, D. Xiong, F. Wei, W. G. Song, J. Xu, L. Liu, *Adv. Energy Mater.* **2017**, *7*, 1602579.
- [38] Z. Wang, J. Li, X. Tian, X. Wang, Y. Yu, K. A. Owusu, L. He, L. Mai, *ACS Appl. Mater. Interfaces* **2016**, *8*, 19386.
- [39] J. Li, D. Fan, M. Wang, Z. Wang, Z. Liu, K. Zhao, L. Zhou, L. Mai, *ChemElectroChem* **2018**, DOI: 10.1002/celec.201801316.
- [40] Y. Sun, K. Xu, Z. Wei, H. Li, T. Zhang, X. Li, W. Cai, J. Ma, H. J. Fan, Y. Li, *Adv. Mater.* **2018**, *30*, 1802121.
- [41] C. Xia, Q. Jiang, C. Zhao, M. N. Hedhili, H. N. Alshareef, *Adv. Mater.* **2016**, *28*, 77.
- [42] A. Grimaud, K. J. May, C. E. Carlton, Y.-L. Lee, M. Risch, W. T. Hong, J. Zhou, S.-H. Yang, *Nat. Commun.* **2013**, *4*, 2439.
- [43] M. T. Koper, *J. Electroanal. Chem.* **2011**, *660*, 254.
- [44] T. Take, K. Tsurutani, M. Umeda, *J. Power Sources* **2007**, *164*, 9.
- [45] L. Dai, Q. Qin, X. Zhao, C. Xu, C. Hu, S. Mo, Y. O. Wang, S. Lin, Z. Tang, N. Zheng, *ACS Cent. Sci.* **2016**, *2*, 538.
- [46] Z. Pu, I. S. Amiinu, F. Gao, Z. Xu, C. Zhang, W. Li, G. Li, S. Mu, *J. Power Sources* **2018**, *401*, 238.
- [47] S. Chen, J. Duan, A. Vasileff, S. Z. Qiao, *Angew. Chem. Int. Ed.* **2016**, *55*, 3804.
- [48] Z.-Y. Yu, C.-C. Lang, M.-R. Gao, Y. Chen, Q.-Q. Fu, Y. Duan, S.-H. Yu, *Energy Environ. Sci.* **2018**, *11*, 1890.
- [49] C. Li, Y. Liu, Z. Zhuo, H. Ju, D. Li, Y. Guo, X. Wu, H. Li, T. Zhai, *Adv. Energy Mater.* **2018**, 1801775.

- [50] J.-Y. Zhang, X. Tian, T. He, S. Zaman, M. Miao, Y. Yan, K. Qi, Z. Dong, H. Liu, B. Y. Xia, *J. Mater. Chem. A* **2018**, 6, 15653.
- [51] F. Li, J. Chen, D. Zhang, W.-F. Fu, Y. Chen, Z. Wen, X.-J. Lv, *Chem. Commun.* **2018**, 54, 5181.
- [52] B. You, N. Jiang, X. Liu, Y. Sun, *Angew. Chem.* **2016**, 128, 10067.
- [53] J. Y. Zhang, H. Wang, Y. Tian, Y. Yan, Q. Xue, T. He, H. Liu, C. Wang, Y. Chen, B. Y. Xia, *Angew. Chem. Int. Ed.* **2018**, DOI: 10.1002/ange.201803543.
- [54] J. Wang, X. Ma, T. Liu, D. Liu, S. Hao, G. Du, R. Kong, A. M. Asiri, X. Sun, *Mater. Today Energy* **2017**, 3, 9.
- [55] L. S. Wu, H. B. Dai, X. P. Wen, P. Wang, *ChemElectroChem* **2017**, 4, 1944.
- [56] Y. Hao, Y. Xu, W. Liu, X. Sun, *Mater. Horiz.* **2018**, 5, 108.
- [57] Q. Qin, H. Jang, P. Li, B. Yuan, X. Liu, J. Cho, *Adv. Energy Mater.* **2018**, 1803312.
- [58] V. Rosca, M. T. Koper, *Electrochim. Acta* **2008**, 53, 5199.
- [59] Y. Liang, Y. Zhou, J. Ma, J. Zhao, Y. Chen, Y. Tang, T. Lu, *Appl. Catal., B* **2011**, 103, 388.
- [60] K. Asazawa, K. Yamada, H. Tanaka, M. Taniguchi, K. Oguro, *J. Power Sources* **2009**, 191, 362.
- [61] H. Wang, Y. Ma, R. Wang, J. Key, V. Linkov, S. Ji, *Chem. Commun.* **2015**, 51, 3570.
- [62] X. Ma, J. Wang, D. Liu, R. Kong, S. Hao, G. Du, A. M. Asiri, X. Sun, *New J. Chem.* **2017**, 41, 4754.
- [63] C. Tang, R. Zhang, W. Lu, Z. Wang, D. Liu, S. Hao, G. Du, A. M. Asiri, X. Sun, *Angew. Chem.* **2017**, 129, 860.
- [64] L. Zhang, D. Liu, S. Hao, L. Xie, F. Qu, G. Du, A. M. Asiri, X. Sun, *ChemistrySelect* **2017**, 2, 3401.
- [65] M. Liu, R. Zhang, L. Zhang, D. Liu, S. Hao, G. Du, A. M. Asiri, R. Kong, X. Sun, *Inorg. Chem. Front.* **2017**, 4, 420.
- [66] Q. Shao, P. Wang, X. Huang, *Adv. Funct. Mater.* **2018**, 1806419.
- [67] B. Zhang, J. Liu, J. Wang, Y. Ruan, X. Ji, K. Xu, C. Chen, H. Wan, L. Miao, J. Jiang, *Nano Energy* **2017**, 37, 74.
- [68] P. Chen, Y. Tong, C. Wu, Y. Xie, *Acc. Chem. Res.* **2018**, 51, 2857.
- [69] X. Cui, P. Xiao, J. Wang, M. Zhou, W. Guo, Y. Yang, Y. He, Z. Wang, Y. Yang, Y. Zhang, Z. Lin, *Angew. Chem. Int. Ed.* **2017**, 56, 4488.
- [70] B. Qiu, L. Cai, Y. Wang, Z. Lin, Y. Zuo, M. Wang, Y. Chai, *Adv. Funct. Mater.* **2018**, 28, 1706008.

- [71] L. Cai, B. Qiu, Z. Lin, Y. Wang, S. Ma, M. Wang, Y. H. Tsang, Y. Chai, *J. Mater. Chem. A* **2018**, 6, 21445.
- [72] B. Qiu, L. Cai, Y. Wang, S. Ma, Y. H. Tsang, Y. Chai, *Mater. Today Energy* **2019**, 11, 89.
- [73] J. Balamurugan, C. Li, T. D. Thanh, O.-K. Park, N. H. Kim, J. H. Lee, *J. Mater. Chem. A* **2017**, 5, 19760.
- [74] A. D. Jagadale, G. Guan, X. Li, X. Du, X. Ma, X. Hao, A. Abudula, *J. Power Sources* **2016**, 306, 526.
- [75] T. Liu, A. Li, C. Wang, W. Zhou, S. Liu, L. Guo, *Adv. Mater.* **2018**, 30, 1803590.
- [76] Y. Hou, M. Qiu, G. Nam, M. G. Kim, T. Zhang, K. Liu, X. Zhuang, J. Cho, C. Yuan, X. Feng, *Nano Lett.* **2017**, 17, 4202.
- [77] H. J. Song, H. Yoon, B. Ju, G. H. Lee, D. W. Kim, *Adv. Energy Mater.* **2018**, 1802319.
- [78] Q. Hu, X. Liu, B. Zhu, L. Fan, X. Chai, Q. Zhang, J. Liu, C. He, Z. Lin, *Nano Energy* **2018**, 50, 212.
- [79] X. Wang, W. Li, D. Xiong, D. Y. Petrovykh, L. Liu, *Adv. Funct. Mater.* **2016**, 26, 4067.
- [80] P. W. Menezes, C. Panda, S. Loos, F. Bunschei-Bruns, C. Walter, M. Schwarze, X. Deng, H. Dau, M. Driess, *Energy Environ. Sci.* **2018**, 11, 1287.
- [81] M. Kuang, P. Han, L. Huang, N. Cao, L. Qian, G. Zheng, *Adv. Funct. Mater.* **2018**, 1804886.
- [82] Q. Li, Z. Xing, D. Wang, X. Sun, X. Yang, *ACS Catal.* **2016**, 6, 2797.
- [83] B. Hammer, J. K. Nørskov, *Nature* **1995**, 376, 238.
- [84] Y. Pan, K. Sun, Y. Lin, X. Cao, Y. Cheng, S. Liu, L. Zeng, W.-C. Cheong, D. Zhao, K. Wu, Z. Liu, Y. Liu, D. Wang, Q. Peng, C. Chen, Y. Li, *Nano Energy* **2019**, 56, 411.
- [85] J. Greeley, J. K. Nørskov, M. Mavrikakis, *Annu. Rev. Phys. Chem.* **2011**, 53, 319.
- [86] C. Meng, T. Ling, T. Y. Ma, H. Wang, Z. Hu, Y. Zhou, J. Mao, X. W. Du, M. Jaroniec, S. Z. Qiao, *Adv. Mater.* **2017**, 29, 1604607.
- [87] F. Song, W. Li, J. Yang, G. Han, P. Liao, Y. Sun, *Nat. Commun.* **2018**, 9, 4531.

Table of Contents

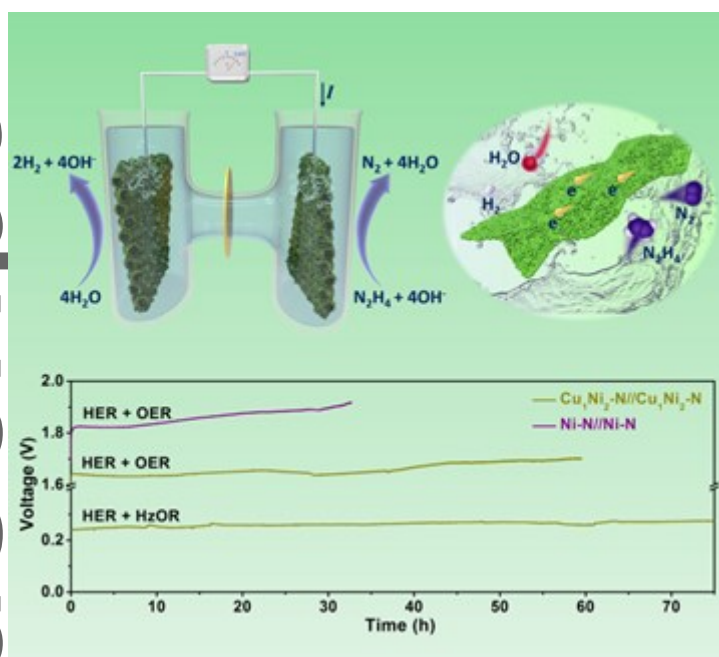
This article is protected by copyright. All rights reserved.

A new type copper-nickel nitride porous nanosheets with rich Ni₃N/Cu₄N interface supported on the carbon fiber cloth is synthesized for the first time. The bifunctional catalyst electrode exhibits both outstanding performance for hydrogen evolution reaction and hydrazine oxidation reaction, making it a promising candidate for energy saving electrolytic hydrogen production.

Keyword: water electrolysis, bifunctional catalysts, copper-nickel nitride, hydrogen evolution, hydrazine oxidation

Zhaoyang Wang, Lin Xu, Fuzhi Huang,* Longbing Qu, Jiantao Li, Kwadwo Asare Owusu, Ziang Liu, Zifeng Lin, Binhua Xiang, Xiong Liu, Kangning Zhao, Xiaobin Liao, Wei Yang, Yi-Bing Cheng, Liqiang Mai*

Title: Copper-Nickel Nitride Nanosheets as Efficient Bifunctional Catalysts for Hydrazine-assisted Electrolytic Hydrogen Production



This article is protected by copyright. All rights reserved.



Minerva Access is the Institutional Repository of The University of Melbourne

Author/s:

Wang, Z;Xu, L;Huang, F;Qu, L;Li, J;Owusu, KA;Liu, Z;Lin, Z;Xiang, B;Liu, X;Zhao, K;Liao, X;Yang, W;Cheng, Y-B;Mai, L

Title:

Copper-Nickel Nitride Nanosheets as Efficient Bifunctional Catalysts for Hydrazine-Assisted Electrolytic Hydrogen Production

Date:

2019-06-05

Citation:

Wang, Z., Xu, L., Huang, F., Qu, L., Li, J., Owusu, K. A., Liu, Z., Lin, Z., Xiang, B., Liu, X., Zhao, K., Liao, X., Yang, W., Cheng, Y. -B. & Mai, L. (2019). Copper-Nickel Nitride Nanosheets as Efficient Bifunctional Catalysts for Hydrazine-Assisted Electrolytic Hydrogen Production. *ADVANCED ENERGY MATERIALS*, 9 (21), <https://doi.org/10.1002/aenm.201900390>.

Persistent Link:

<http://hdl.handle.net/11343/285627>